SCIENCE CHINA Materials ARTICLES

mater.scichina.com link.springer.com

Published online 19 March 2020 | https://doi.org/10.1007/s40843-019-1272-0
Sci China Mater 2020, 63(6): 1085–1098

Insights into the deep-tissue photothermal therapy in near-infrared II region based on tumor-targeted MoO_2 nanoaggregates

Yanxian Guo[1], Yang Li[1], Wolun Zhang[1], Hongru Zu[2], Haihong Yu[1], Dongling Li[1], Honglian Xiong[3], Tristan T. Hormel[4], Chaofan Hu[2*], Zhouyi Guo[1*] and Zhiming Liu[1*]

ABSTRACT Research on deep-tissue photothermal therapy (PTT) in the near-infrared II (NIR-II, 1000–1350 nm) region has bloomed in recent years, owing to higher maximum permissible exposure and deeper tissue penetration over that in the near-infrared I (NIR-I, 650–950 nm) region. However, more details need to be uncovered to facilitate a fundamental understanding of NIR-II PTT. Herein, a tumor-targeted therapeutic nanosystem based on NIR-responsive molybdenum oxide (MoO_2) nanoaggregates was fabricated. The photothermal conversion capabilities of MoO_2 in the NIR-I and II regions were investigated step by step, from a simple tissue phantom to a three-dimensional cellular system, and further to a tumor-bearing animal model. NIR-II laser exhibited a lower photothermal attenuation coefficient (0.541 at 1064 nm) in a tissue phantom compared with its counterpart (0.959 at 808 nm), which allows it to be more capable of deep-tissue PTT *in vitro* and *in vivo*. Depth profile analysis elucidated a negative correlation between the microstructural collapse of tumor tissue and the penetration depth. Moreover, the depth-related tumor ablation was also studied by Raman fingerprint analysis, which demonstrated the major biochemical compositional disturbances in photothermal ablated tumor tissues, providing fundamental knowledge to NIR-II deep-tissue photothermal therapy.

Keywords: second near-infrared window, photothermal therapy, molybdenum oxide, depth profile analysis, Raman biochemical assay

INTRODUCTION

Novel therapeutic strategies to deal with deep-seated tumors have attracted extensive interest recently [1–3]. Photothermal tumor therapy using the excitation source at the near-infrared II (NIR-II) region with a wavelength of 1000–1350 nm, which exhibits deeper tissue penetration, lower background noise and higher maximum permissible exposure (MPE), has been considered as more appealing for deep-tissue tumors relative to traditional NIR-I photothermal therapy (PTT). According to the America National Standards for Safe Use of Lasers, MPE for skin exposure to NIR-I laser (808 nm) is 0.33 W cm^{-2}, while that to NIR-II laser (1064 nm) is 1 W cm^{-2} (ANSI Z136.1-2007), allowing a wider applicability of NIR-II-responsive photothermal agents [4]. Nowadays, several materials including inorganic nanomaterials [5–10], small organic molecule-based nanoparticles [11–13] and semiconducting polymer nanoparticles [14–20] have been explored as therapeutic agents for efficient NIR-II photothermal tumor ablation *in vitro* and *in vivo*. Though an excellent antitumor effect has been achieved, the tumor depth profiles after NIR-II PTT are rarely systematically studied.

Transition metal oxide (TMO) semiconductor nanomaterials have been attracting great attention in recent years owing to superior biocompatibility, easy preparation and flexibly tailored localized surface plasmon resonance (LSPR) effect [21,22]. Especially, more interest has been focused on the broadband absorbing TMOs and their derivatives for NIR-II PTT [23–25]. However, most

[1] Guang Provincial Key Laboratory of Laser Life Science & SATCM Third Grade Laboratory of Chinese Medicine and Photonics Technology, College of Biophotonics, South China Normal University, Guangzhou, 510631, China
[2] Guangdong Provincial Engineering Technology Research Center for Optical Agriculture, College of Materials and Energy, South China Agricultural University, Guangzhou 510642, China
[3] Department of Physics and Optoelectronic Engineering, Foshan University, Foshan 528000, China
[4] Casey Eye Institute, Oregon Health and Science University, Portland, 97239 Oregon, USA
[*] Corresponding authors (emails: thucf@scau.edu.cn (Hu C); ann@scnu.edu.cn (Huo Z); liuzm021@126.com (Liu Z))

 © Science China Press and Springer-Verlag GmbH Germany, part of Springer Nature 2020

of the reported TMOs suffer from relatively low photothermal conversion efficiencies (PTCEs) in NIR-II region. As an emerging type of NIR plasmonic semiconductor, oxygen-deficient molybdenum oxides (MoO_x, $2 \leq x < 3$) have seen a remarkable burst of interest due to the low-cost synthesis, tunable band gap and pH-dependent oxidative degradation [26–28]. For example, Yin *et al.* [29] synthesized small-sized MoO_x nanoparticles with a wide light absorption from 600 to 1200 nm using the facile hydrothermal method. An appropriate PTCE of MoO_x nanoparticles was calculated to be 37.4% at 1064 nm, while that at 808 nm was 27.3%, which allowed a superior tumor inhibition in the NIR-II region. The hydrothermal strategy also allows MoO_x nanostructures with various morphologies which exhibit controlled LSPR absorption for effective NIR photothermal ablation of cancer cells [30]. In addition, MoO_x is also a pH-dependent biodegradable nanomaterial that can be readily degraded in normal organs but is relatively stable in tumors, indicating the selective tumor-killing capacity of MoO_x-based therapeutic nanosystems [31]. However, in the issue of deep-seated tumors, only spare details after MoO_x-based PTT can be ferreted out in these literature studies.

Herein, we developed a facile and green method to fabricate MoO_2 nanoaggregates as a novel photothermal agent for highly efficient *in-vivo* photothermal ablation of mouse tumor xenografts at both NIR-I and NIR-II windows (Scheme 1). The nanoaggregates were further functionalized with polyethylene glycol (PEG) and hyaluronic acid (HA) to allow better physiological stability and tumor-targeted capability. The obtained MoO_2@PEG@HA (MPH) exhibited an excellent photothermal performance across NIR-I and NIR-II regions. The comparative antitumor PTT experiments between the two NIR regions were then carried out *in vitro* and *in vivo*. We also investigated the deep-tissue profiles of the tumors after PTT in order to understand the fundamental features of NIR-II PTT based on MoO_2-related nanomaterials.

EXPERIMENTAL SECTION

Materials

Ammonium molybdate tetrahydrate ($(NH_4)_6Mo_7O_{24}\cdot 4H_2O$, AMT) and polyvinyl pyrrolidone (PVP, molecular weight = 10,000) were obtained from Aladdin Industrial Corporation (Shanghai, China). Eight arm amino polyethylene glycol (8 arm-PEG-NH_2) was purchased from Xi'an ruixi Biological Technology Co. HA, sulforhodamine B (SRB), trichloroacetic acid (TCA), tris-hydroxymethyl-aminomethane (Tris) were provided by Aladdin (Shanghai, China). Dulbecco's modified Eagle's medium (DMEM, high glucose) and fetal bovine serum (FBS) were obtained from GIBCO (Grand Island, NY, United States). Gelatin from porcine skin, Calcien AM, and propidium iodide (PI) were obtained from Sigma-Aldrich. All reagents were used without further purification. Deionized water (Milli-Q System, Millipore, USA) was used in all experiments.

Preparation of MoO_2 nanoaggregates

MoO_2 nanoaggregates can be synthesized *via* a one-pot hydrothermal method. In detail, 0.1 mol of $(NH_4)_6Mo_7O_{24}\cdot 4H_2O$ was dissolved in 26 mL of water by ultrasonication. After that, 2.5 mL of 3 mol L^{-1} HCl and 3.76 g of PVP, the reducing agent, were added into the solution and kept at room temperature for 30 min. The mixture was transferred to a 50-mL Teflon-lined stainless steel autoclave and heated to 240°C for 12 h. Once cooled down to room temperature, the solution was centrifuged at 1500 rpm for 8 min to remove the over-size MoO_2. The resulting suspension of molybdenum oxide nanomaterials was then dialyzed against deionized water for 48 h by

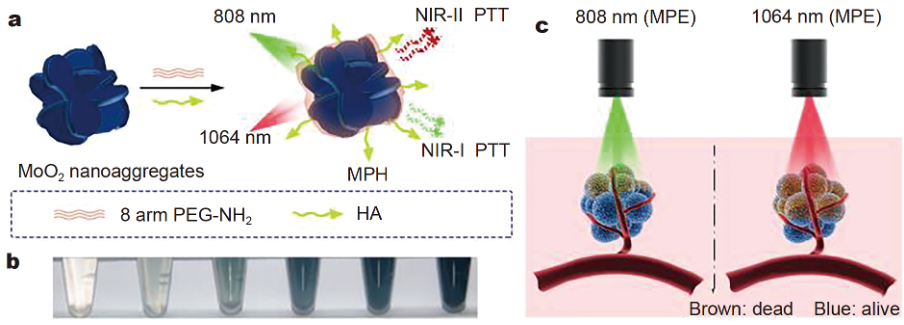

Scheme 1 Schematic illustration of the NIR-responsive MoO_2 nanoaggregates and their photothermal therapeutic applications. (a) Surface modification of MoO_2 nanoaggregates. (b) Photographs of MPH aqueous suspensions at varying concentrations (0, 50, 100, 200, 300, 500 μg mL^{-1}). (c) Illustration of the deep-tissue PTT under MPE of NIR-I and NIR-II irradiation.

© Science China Press and Springer-Verlag GmbH Germany, part of Springer Nature 2020

using a 3500-Da dialysis bag. Subsequently, the collected suspension was freeze-dried, and the prepared MoO_2 powder was finally resuspended in deionized water for further use.

Preparation of MoO_2@PEG@HA

8 arm PEG-NH_2 and HA were grafted to MoO_2 nanoaggregates by electrostatic bonding and amide reaction, respectively. 40 mg of 8 arm PEG-NH_2 and 20 mg of MoO_2 were dissolved in water and kept mixing for 4 h, then centrifuged at 3500 rpm for 20 min (performed three times) to collect the pure PEG-MoO_2. 100 mg HA, 310 mg NHS and 188 mg *N*-ethyl-*N*′-(3-dimethylaminopropyl)carbodiimide were mixed for 2 h to activate carboxyl. PEG-MoO_2 was added to HA solution and stirred overnight. The solution was centrifuged and freeze-dried to get the MPH powder.

Characterization

The ultraviolet visible NIR (UV-Vis-NIR) spectra of the nanocomposites were taken by an absorption spectrometer (UV-6100S, MAPADA, China). Transmission electron microscopy (TEM) analysis was performed by a JEM-2010HR transmission electron microscope (JEOL, Japan) at an accelerating voltage of 200 kV, equipped with an energy-dispersive X-ray (EDX) spectrometer. Scanning electron microscopy (SEM) analysis was carried out by using a Verios 460 field-emission scanning electron microscope (Thermo Fisher, USA). X-ray diffraction (XRD) spectra were recorded with a Bruker D8 focus X-ray diffractometer by CuKα radiation (λ = 1.54051 Å). Raman spectra were collected by using Renishaw inVia microspectrometer (Derbyshire, England) under a 785-nm diode laser excitation and coupled to a Leica DM-2500M microscope (Leica Microsystems GmbH, Wetzlar, Germany). The Nicolet 6700 Fourier transformed infrared (FT-IR) Spectrometer was used to obtain the FT-IR spectrum. X-ray photoelectron spectroscopy (XPS) spectra were measured by Thermo Scientific Escalab 250 Xi photoelectron spectroscopy. The zeta potential and hydrodynamic diameter of nanomaterials were measured on Malvern Zetasizer Nano ZS analyzer.

Photothermal effect of MPH

The MPH suspension was diluted to different concentration for further analysis.

Calculation of the extinction coefficient

The NIR absorption capability of MPH was tested by an absorption spectrometer. The extinction coefficients (ε) at 808 and 1064 nm were determined according to the Lambert-Beer law:

$$A_\lambda = \varepsilon LC,$$

where A_λ means the absorbance at a wavelength of λ, L is pathlength (cm), C is the concentration of MPH solution (in g L^{-1}), and ε is calculated by plotting the slope of each linear fit against wavelength.

Calculation of the photothermal conversion efficiency

MPH (200 μg mL^{-1}) was irradiated with the representative NIR-I and NIR-II laser for 6 min, followed by the natural cooling procedure. The temperature of the solutions was measured every 30 s by using an infrared thermal camera (Fluke Ti200, Fluke Corp, USA). The PTCEs (η) at 1064 and 808 nm were calculated by using the following equation:

$$\eta = \frac{hS(T_{\max} - T_{\text{surr}}) - Q_{\text{dis}}}{I(1 - 10^{-A_\lambda})},$$

$$\tau_s = \frac{m_{\text{D}} C_{\text{D}}}{hS},$$

where h is the heat transfer coefficient, S is the surface area of the container, I expresses the NIR laser power (1 W cm^{-2}), A_λ means the absorbance at λ of the nanostructures (optical density: OD_{808} = 1.54, OD_{1064} = 1.72), $T_{\max}$ is the equilibrium temperature, T_{surr} is the ambient temperature of the surroundings, and Q_{dis} is the heat associated with the light absorbance by the solvent. τ_s represents the sample system time constant, m_{D} and C_{D} mean the mass (1.2 g was used) and heat capacity (4.2 J g^{-1}), when pure water is used as the solvent. Pure water in a test tube was applied to measure the Q_{dis}.

Hemolysis assay

Human blood obtained from healthy volunteers was centrifuged at 3000 rpm for 5 min and washed several times with normal saline to obtain pure erythrocytes. Then, 4% of erythrocytes (v/v) was mixed with the same volume of water (positive control), normal saline (negative control) or MPH solution at various concentrations. The mixture was incubated at 37°C for 3 h. After centrifugation, the supernatants were collected, and the absorbance at 541 nm was recorded by using a UV-Vis-NIR spectrophotometer. The percentage of hemolysis was calculated by using the following equation:

$$\text{Hemolysis}(\%) = \frac{(A_{\text{sample}} - A_{\text{negative control}})}{(A_{\text{positive control}} - A_{\text{negativecontrol}})} \times 100\%.$$

Cytotoxicity assay

Human lung cancer A549 cells line (noted as A549 cells)

 © Science China Press and Springer-Verlag GmbH Germany, part of Springer Nature 2020

and human lung LO2 normal cell (noted as LO2 cells) were maintained at 37°C under 5% CO_2 in DMEM and supplemented with 1% penicillin/streptomycin and 10% FBS in a humidified incubator. To avoid the interference of reducibility of nanocomposites, the cytotoxicity of MPH in different concentrations was tested by using SRB (a dye binding to cellular proteins) assay. A549 cells and LO2 cells were plated in 96-well plates (Corning), allowed to adhere overnight, and then culture medium above was changed with fresh culture medium containing MPH at different concentrations (0, 25, 50, 75, 100, 200, 300 and 500 μg mL^{-1}). After 24 h of incubation, cells were fixed by 10% trichloroacetic acid for 1 h at 4°C. After fixation, cells were washed twice with water and incubated with SRB (0.4% *w*/*v* in 1% acetic acid) for 30 min at room temperature, followed by four washes with 1% acetic acid. The bound dye was solubilized in 1 mL of 10 mmol L^{-1} Tris base solution and the absorbance was measured at 565 nm. Cell viability results were expressed as percentage of viable cells in treated samples with respect to controls (n = 6). All the experiments were performed in triplicate and repeated three times.

In vitro PTT in NIR-I and NIR window

Briefly, A549 cells were seeded on 96-well plate with a concentration of 100,000 cells/well. After overnight incubation, 100 μL MPH (100 μg mL^{-1}) was incubated with A549 cells for 24 h and irradiated by 808 or 1064 nm at their respective MPE density for 10 min under varying thickness (0, 3, 5, 10, 15, 20 mm). After incubation for another 24 h, the photothermal cytotoxicity was evaluated by the SRB assay as described above.

Three-dimension HA-Gel scaffolds were prepared by a previously reported method [32]. Approximately 1×10^6 cells were seeded on the HA-Gel scaffold. After an 8-day incubation at 37°C in an atmosphere of 5% CO_2 and 95% air incubator, MPH (100 μg mL^{-1}) was incubated with cells for 24 h. Laser irradiation at 1 W cm^{-2} was applied on the top of the HA-Gel scaffold for 2 min and the scaffold was further incubated for 24 h. As for the observation of cell apoptosis along with depth by fluorescence imaging, HA-Gel scaffolds were stained with Calcein-AM and PI solution for 20 min, and frozen at −20°C for 12 h. Freezing microtome sectioning was performed by a cryostat (Leica) for 15 μm slides and then imaged with fluorescence microscope with an extinction wavelength of 495 nm for Calcein-AM and 530 nm for PI.

Mouse tumor model

Female BALB/c nude mice (4 weeks old) were purchased from the Laboratory Animal Center of Sun Yat-sen University and performed with protocols approved by South China Normal University Animal Care and Use Committee. For deep tissue PTT, A549 cells (5×10^7) suspended in 50 μL phosphate buffer saline (PBS) were implanted into the bilateral dorsal subcutis of nude mice. For PTT in NIR-II window, the tumors were established on nude mice by injection of A549 cells (5×10^7) suspended in 50 μL PBS into the left leg of the mice. Tumors were grown until the volume was about 200 mm^3, or a single aspect reached ~10 mm before being used for photothermal treatment.

In vivo PTT in NIR-I and NIR window

Nude mice bearing A549 xenograft tumors were intratumorally injected with MPH solution (1 mg kg^{-1}) and randomly divided into five groups: (1) Control, (2) MPH, (3) 1064 nm; (4) MPH+1064 nm, 1 W cm^{-2}; (5) MPH+808 nm, 0.33 W cm^{-2}. All laser irradiation was conducted with 3 mm tissue covered for 10 min. All mice were anesthetized by pentobarbital sodium before NIR irradiation. The measurement of tumor volume was conducted by vernier calipers every 2 days for 16 days after treatments. The tumor volume was measured by using the following equation: tumor volume = 0.5 × (tumor length) × (tumor width)^2. Relative tumor volume was quantified as V/V_0, where V_0 was the initial tumor volume. The tumors and organs of mice were collected for H&E (Hematoxylin and Eosin) staining.

Nude mice bearing A549 xenograft tumors reaching 10 mm were intratumorally injected with MPH solution (1 mg kg^{-1}). Tumors were irradiated by 808 and 1064 nm at 1 W cm^{-2} for 2 min on the longitudinal side. The tumors of 10 mm were longitudinal sliced at maximum cross section for TUNEL staining and transverse sliced every 1 mm for H&E and Ki-67 staining according to standard protocols, then examined under the microscope. For surface-enhanced Raman scattering (SERS) analysis, the transverse sliced tumors were immersed into the SERS substrate solution, after which the slices were rinsed with ultrapure water three times. Raman spectroscopic measurements of tumor sections were performed along the depth. The 63× water immersion objective lens (NA = 0.9) and 50× objective were chosen for tissue detection. Raman spectral mapping was performed in the streamline mode at wavenumber center 1200 cm^{-1}.

In vivo NIR-II PTT

Nude mice bearing xenograft A549 tumors were intravenously injected with MPH solution (1 mg kg^{-1}) and

 © Science China Press and Springer-Verlag GmbH Germany, part of Springer Nature 2020

randomly divided into two groups: (1) 1064 nm; (2) MPH +1064 nm. All mice were anesthetized by trichloracetic aldehyde before NIR irradiation. The measurements of tumors' volume were conducted by vernier calipers every 2 days during 16 days after the corresponding treatments. The tumor volume was measured, and the relative tumor volume was quantified as described above. The tumors and organs of mice were collected for H&E staining.

In vivo toxicity

Six mice were divided into two groups: (1) control group, (2) mice intravenously administered with MPH (5 mg mL^{-1}). The histological, hematological, and blood biochemical indices were collected at varied time intervals of 1, 7 and 16 days after intravenous administration. At Day 16 after treatment, the organs were separated for H&E staining for observation.

RESULTS AND DISCUSSION

MoO_2 nanoaggregates with deep-dark-blue color were synthesized successfully by a simple hydrothermal process using PVP as the reductant and stabilizer (Fig. S1a). The XRD pattern (Fig. S1b) of MoO_2 nanoaggregates shows a typical monoclinic phase of molybdenum oxide (JCPDS No. 32-0671) with standard lattice parameters of a = 5.6068 Å, b = 4.8595 Å, c = 5.5373 Å. No diffraction peaks for MoO_3 or other crystalline phases are found, suggesting that the synthetic powder is phase-pure MoO_2. Then, the morphologies of MoO_2 nanoaggregates were examined by TEM, which displayed the flower-like nanostructures around 100 nm consisted of a few small quasi-circular particles (~20 nm, Fig. S1c). The high resolution TEM (HRTEM) image and the corresponding selected–area electron diffraction (SAED) pattern clearly show a high degree of crystallinity of MoO_2 nanoaggregates (Fig. S1d and inset). The spacing of the lattice fringe of 0.24 and 0.48 nm can be severally indexed to the (111) and (101) planes of monoclinic MoO_2 [33]. EDX spectroscopy coupled with TEM suggests the existence of Mo and O elements in the nanostructures (Fig. S1e). Strong intraparticle plasmonic coupling among nanoaggregates in close proximity leads to uniform broadband absorption spanning in the 650–1350 nm range (Fig. S1f) [13]. The Raman spectrum of MoO_2 nanoaggregates (Fig. S1g) shows some typical peaks at 993, 820 and 660 cm^{-1}, which can be attributed to the stretching vibrations of terminal oxygen (Mo=O), double coordinated bringing oxygen (Mo_2–O) and triple coordinated bringing oxygen (Mo_3–O) groups, respectively [34,35]. The vibration modes in MoO_2 nanostructures can also be confirmed by the FT-IR spectrum (Fig. S2). Then the valance state of Mo element was investigated by XPS. As exhibited in Fig. S1h, five obvious peaks are detected in the XPS spectra of MoO_2 samples, including Mo 3d (231.8 eV), C 1s (285 eV), Mo $3p_{3/2}$ (401.1 eV), Mo $3p_{1/2}$ (415.1 eV) and O 1s (531.1 eV). In particular, the typical four bands in high resolution XPS spectrum (Fig. S1i) can be ascribed to three spit-orbit doublets, corresponding to Mo^{4+}, Mo^{5+} and Mo^{6+}, respectively. The strong peaks at 229.6 and 232.8 eV can be attributed to Mo^{4+}, while the weak peaks at 230.8 and 234.5 eV are traits of Mo^{6+}, and the weak peaks at 231.6 and 235.7 eV are characteristic of Mo^{5+} [28,32]. The content is determined as 63.2%, 14.3% and 22.5% for Mo^{4+}, Mo^{5+} and Mo^{6+}, respectively. The summed contents of Mo^{4+} and Mo^{5+} are much higher than that of Mo^{6+}, demonstrating that a large proportion of Mo element exists in reduction state.

For tumor-targeted biomedical application, MoO_2 nanoaggregates were functionalized with PEG and HA (MPH). As shown in Fig. 1a, a core-shell morphology of MPH is observed in the TEM image, where MoO_2 nanoaggregates are clearly wrapped by thin film in roughly 2 nm. We can also observe some cross-linked filaments in the SEM images (Fig. 1b and Fig. S3), indicating the successful attachment of polymers. The mean hydrodynamic diameters of MoO_2, MoO_2-PEG and MPH determined by dynamic light scattering are 178, 271 and 293 nm, respectively (Fig. 1c). The surface functionalization can alter the zeta potentials of MoO_2-based nanoparticles that are displayed in Fig. 1c. The typical absorbance peaks of PEG and HA in the UV-Vis-NIR spectrum of MPH also verify the successful grafting of the polymers (Fig. 1d). A concentration-dependent transmittance of MPH is observed in the range of 400–1100 nm; almost all the light is absorbed by the MPH solution at a concentration of ~0.033% (w/w) in Fig. 1e. Following the Lambert-Beer law, the extinction coefficients of MPH at 808 and 1064 nm are calculated as 10.1 and 7.8 L g^{-1} cm^{-1}, respectively (Fig. S4), which elucidate the wide and strong NIR laser absorption capability of MPH. The FT-IR spectrum of MPH is shown in Fig. 1f, where the vibrational modes of the modifiers can be easily noticed [36]. Moreover, the obtained MPH nanoaggregates exhibit significantly improved stability in various physiological solutions, such as PBS, DMEM and FBS, benefiting further applications in the biomedical field (Fig. S5). To investigate the tumor-targeting capability of MPH *in vitro*, CD44 (HA receptor)-positive human non-small cell lung cancer (A549) cells and CD44-negative mouse NIH-3T3 fibroblasts were in-

 © Science China Press and Springer-Verlag GmbH Germany, part of Springer Nature 2020

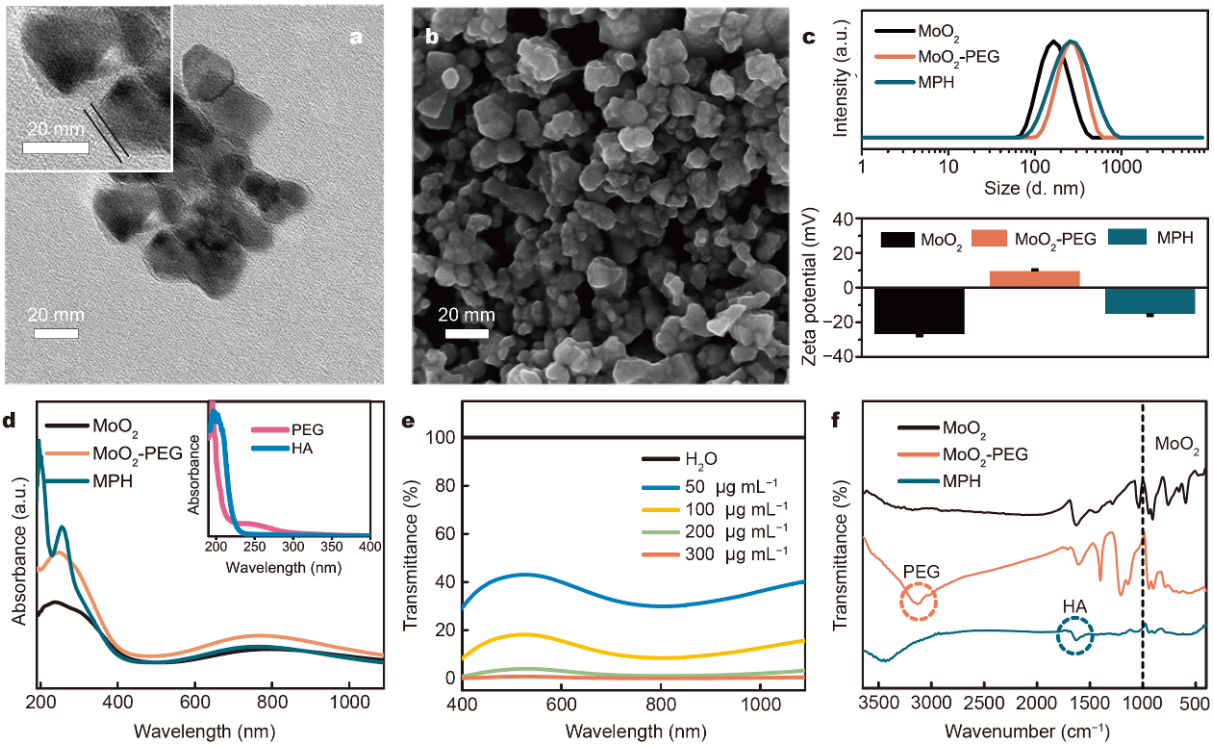

Figure 1 Characterization of MPH. (a) TEM and (b) SEM images of MPH. (c) Zeta potentials and hydrodynamic diameters of the nanomaterials. (d) UV-Vis-NIR absorbance spectra of MoO_2 nanoaggregates after surface modification. (e) Vis-NIR transmittance spectra of MPH at different concentrations. (f) FT-IR spectra of surface-modified MoO_2 nanoaggregates.

cubated with rhodamine B (RhB)-labelled MPH for fluorescence imaging. As shown in Fig. S6, only faint fluorescence is observed in the CD44-negative NIH-3T3 cells, while intense and time-dependent red fluorescence signals are clearly detected in the A549 cells, indicating the massive accumulation of MPH in CD44-positive cancer cells. The specific recognition of CD44 by MPH can be blocked by pre-incubating A549 cells with HA molecules.

The photothermal performance of MPH was then examined in both NIR-I and NIR-II regions by using representative laser wavelengths of 808 and 1064 nm, respectively. Fig. 2a shows the laser power-dependent temperature changes of MPH solutions under laser irradiation. The temperature increase in MPH solution under 1064 nm exposure is similar to that under 808 nm at the same conditions, which can be well demonstrated by the similar heat power density motivated by two wavelengths using three-dimensional finite-difference time-domain (3D FDTD) simulation (inset in Fig. 2a). But at the MPE dose, the ascent rate of temperature under NIR-II laser (1 W cm^{-2}) is significantly higher than that under NIR-I laser (0.33 W cm^{-2}). To accurately describe the photothermal features, η values were calculated based on the previous work [37]. As shown in Fig. 2b, the values are high as 52.9% and 55.6% at 808 and 1064 nm, respectively, showing the advantage of MPH using the NIR-II laser *versus* the NIR-I laser. In addition, the η values of recently reported inorganic PTAs mediated in NIR-II region have been summarized in Table S1, which exhibits that the η of MPH surpasses all TMOs and most of the inorganic PTAs in the literature. A clinical scenario was emulated by utilizing chicken breast as a model tissue to explore the deep tissue photothermal activity. In the presence of chicken tissue (10 mm), more efficient heating is mediated by a 1064 nm laser than by an 808 nm laser (Fig. 2c), which can be attributed to stronger transmittance of the NIR-II laser relative to the NIR-I laser as measured in Fig. 2d. As shown in Fig. 2e, attenuation coefficients (α) of 808 and 1064 nm lasers after passing through the tissue are calculated to be 0.539 and 0.383, respectively, suggesting the deeper tissue penetration of light in NIR-II window. When compared at their respective MPE limits, the temperature changes at 1064 nm are 2.1-, 2.6-, 4.9-, 7.2- and 7.7-fold higher than those at 808 nm at the tissue depths of 3, 5, 10, 15 and

 © Science China Press and Springer-Verlag GmbH Germany, part of Springer Nature 2020

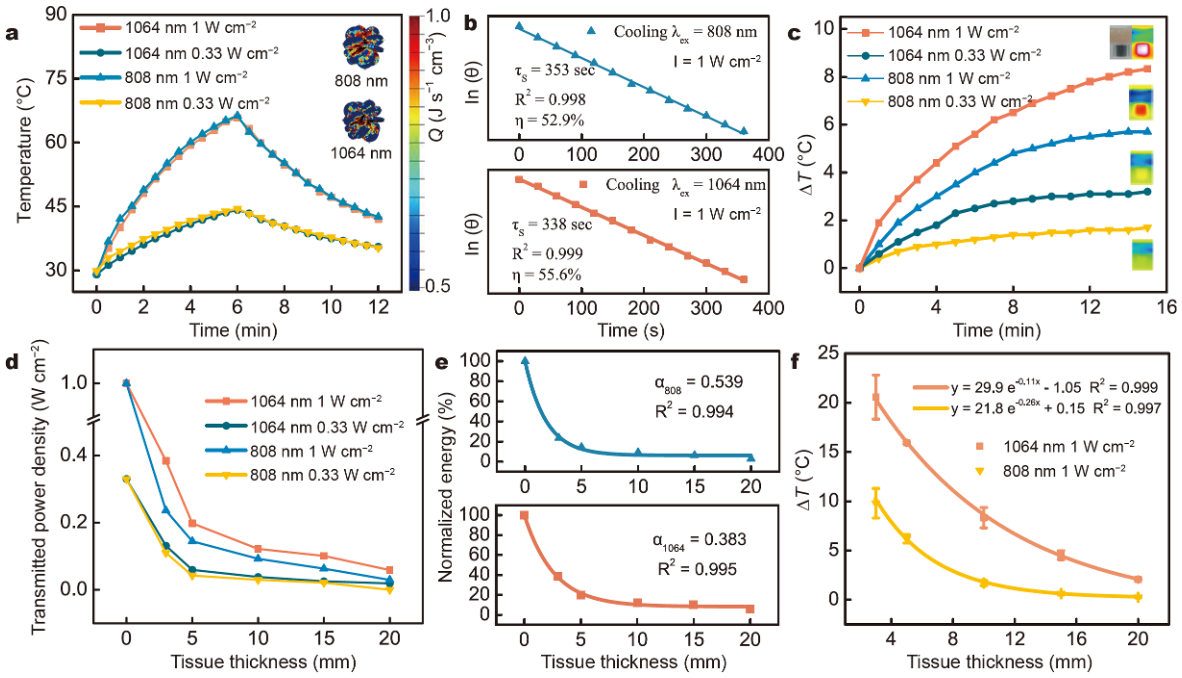

Figure 2 Photothermal performance of MPH. (a) Photothermal heating and cooling curves of MPH (200 μg mL^{-1}) under NIR laser irradiation. Inset: 3D FDTD simulation demonstrates the heat power density Q distribution of the monomer in MPH illuminated by 808 and 1064 nm lasers, respectively. (b) Measuring the time constant for heat transfer from the system by using a linear regression of the cooling profile. (c) Photothermal heating curves of MPH (100 μg mL^{-1}) insulated by 10 mm thick chicken breast tissue. Inset: infrared thermal images and photo of MPH solutions. (d) Transmitted power densities of 808 and 1064 nm under the varied thickness of chicken breast tissue. (e) Normalized penetrated NIR energy through tissues of different depths. α: the attenuation coefficient of NIR laser. (f) Fitted exponential decay of temperature change of MPH (100 μg mL^{-1}) at different thicknesses of chicken breast tissue under two laser conditions.

20 mm, respectively (Fig. 2f). The superior deep tissue photothermal ability at 1064 over 808 nm can be explained as the outcome of intrinsically deeper penetration depth in cooperation with the higher MPH limit in NIR-II range than that in NIR-I range.

The standard SRB assay and hemolysis test were carried out to study the biocompatibility of MPH [38]. MPH shows a negligible effect on A549 cancer cells, LO2 normal liver cells and red blood cells even at a concentration up to 500 μg mL^{-1}, with the cell viabilities more than 85% and hemolysis rate as 2%, respectively (Fig. 3a and Fig. S7). Then *in vitro* deep-tissue cancer ablation was carried out using MPH as the photothermal agent under laser irradiation at MPE doses (1 W cm^{-2} for 1064 nm and 0.33 W cm^{-2} for 808 nm). Chicken breast tissues of various thicknesses were placed between the laser sources and culture plates to simulate different tissue depths. As shown in Fig. 3b, increasing tissue thickness leads to fewer cells being killed owing to weaker energy residuals. Moreover, the NIR-II laser (1064 nm) shows more remarkable photothermal tumor killing performance than the NIR-I laser (808 nm), especially at the tissue thickness of 3 mm. To further verify the superiority of the NIR-II bio-window over the NIR-I bio-window, *in vivo* photothermal ablation experiments were performed on A549 xenograft nude mouse tumor model (Fig. 3c). Tumors with sizes of around 200 mm^3 were divided into five groups: (1) control, (2) MPH, (3) 1064 nm, (4) MPH +808 nm and (5) MPH+1064 nm. The temperature of the tumor during NIR laser irradiation was recorded by infrared thermal imaging. As shown in Fig. 3d, e, the temperatures of the mice tumors increased by 14.2°C after 1064 nm exposure for 10 min, much higher than that irradiated by 808 nm laser (ΔT= 9.8°C), showing a better photothermal conversion effect from the NIR-II laser in deep tissue. Furthermore, *in vivo* photothermal therapeutic outcomes were recorded. Time-dependent tumor growth curves measured with a vernier caliper reveal the lowest growth rate in the MPH+1064 group, which can be viewed as the NIR-II deep-tissue photothermal effect (Fig. 3f). The superior *in vivo* antitumor effect of MPH in NIR-II region can also be visualized in the photographs of mice and the data of *ex vivo* tumors captured 16 days after treatment (Fig. 3g–i). H&E stain-

 © Science China Press and Springer-Verlag GmbH Germany, part of Springer Nature 2020

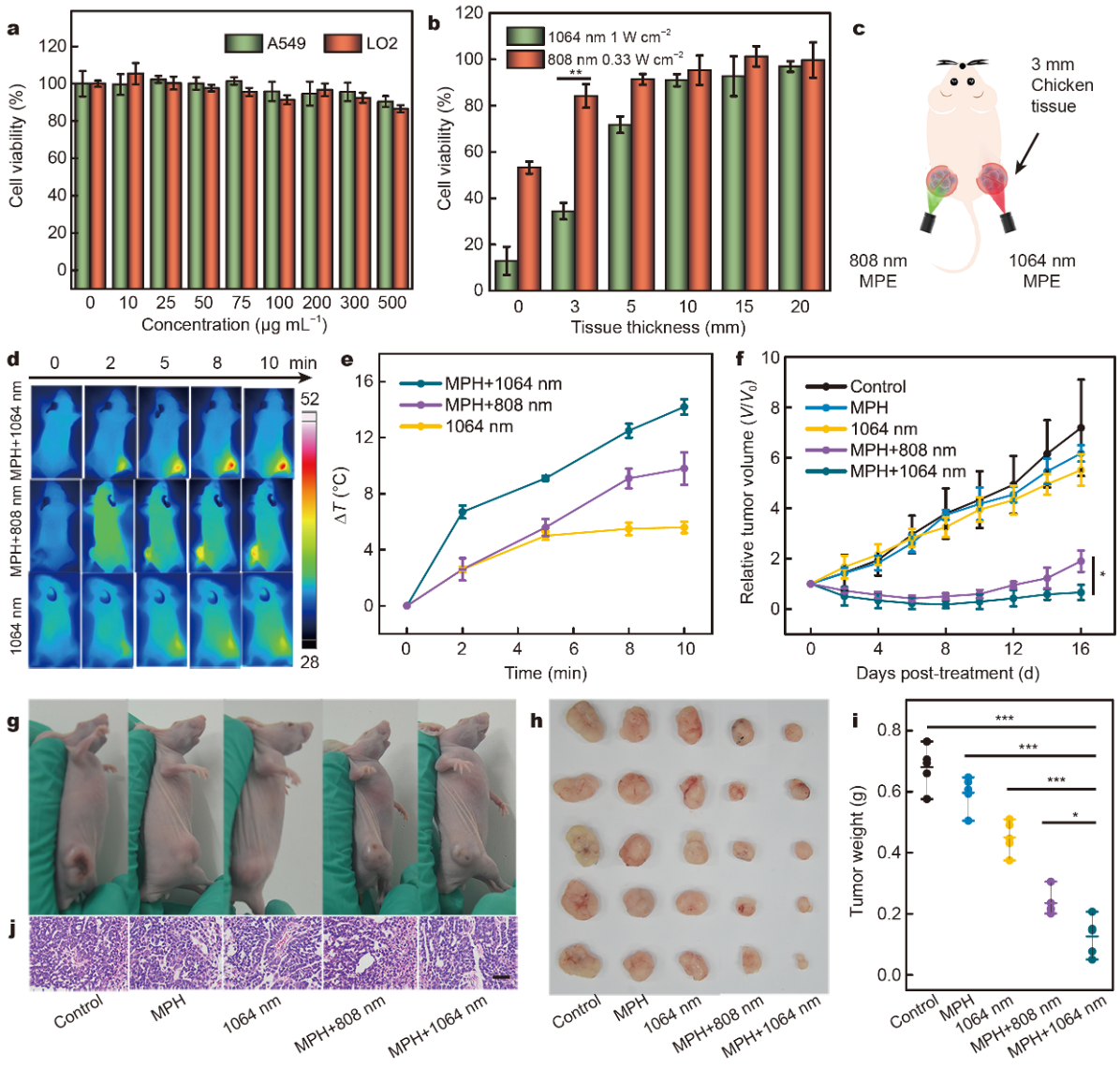

Figure 3 Deep-tissue photothermal tumor ablation in NIR-I and NIR-II windows. (a) Relative viabilities of A549 and LO2 cells after incubation with MPH dispersions at varied concentrations. (b) Relative viability of A549 cells treated with MPH (100 μg mL^{-1}) and NIR lasers in the presence of different thicknesses of chicken breast tissue. (c) Schematic diagram of photothermal cancer therapy on A549-tumor-bearing mice covered by chicken tissue (3 mm). (d) Infrared thermal images of A549-tumor-bearing mice exposed to NIR lasers after intratumor injection with MPH (1 mg mL^{-1}) or saline. (e) Mean temperature changes of tumors along with the irradiation time. (f) Tumor growth curves of mice after different treatments (n = 5). Photographs of (g) tumor-bearing mice and (h) the tumors dissected from mice after different treatments, and (i) tumor weights of mice 16 days after treatment, as well as (j) representative H&E stained images of tumor tissues (Scale bar: 50 μm). * P<0.05, ** P<0.01, *** P<0.001.

ing of tumor slices performed after 24 h of laser treatment shows highly significant cellular necrosis in the MPH +1064 nm laser group (Fig. 3j), further demonstrating the excellent therapeutic efficacy of MPH-based NIR-II PTT *in vivo*.

For detailed investigation, the depth profiles of photothermal-ablated tumors under 808 and 1064 nm lasers were compared. First, a tissue phantom composed of 2% intralipid (IL) was established to mimic the scattering properties of human tissue [39,40]. The concentrations of MPH in IL were adjusted to reach the equal OD values at 808 and 1064 nm. Fig. 4a and Fig. S8 display the infrared thermal images of MPH-contained tissue phantoms under irradiation by the two lasers, where a significantly deeper thermal distribution is observed in the tissue phantom under NIR-II laser exposure. The temperature

 © Science China Press and Springer-Verlag GmbH Germany, part of Springer Nature 2020

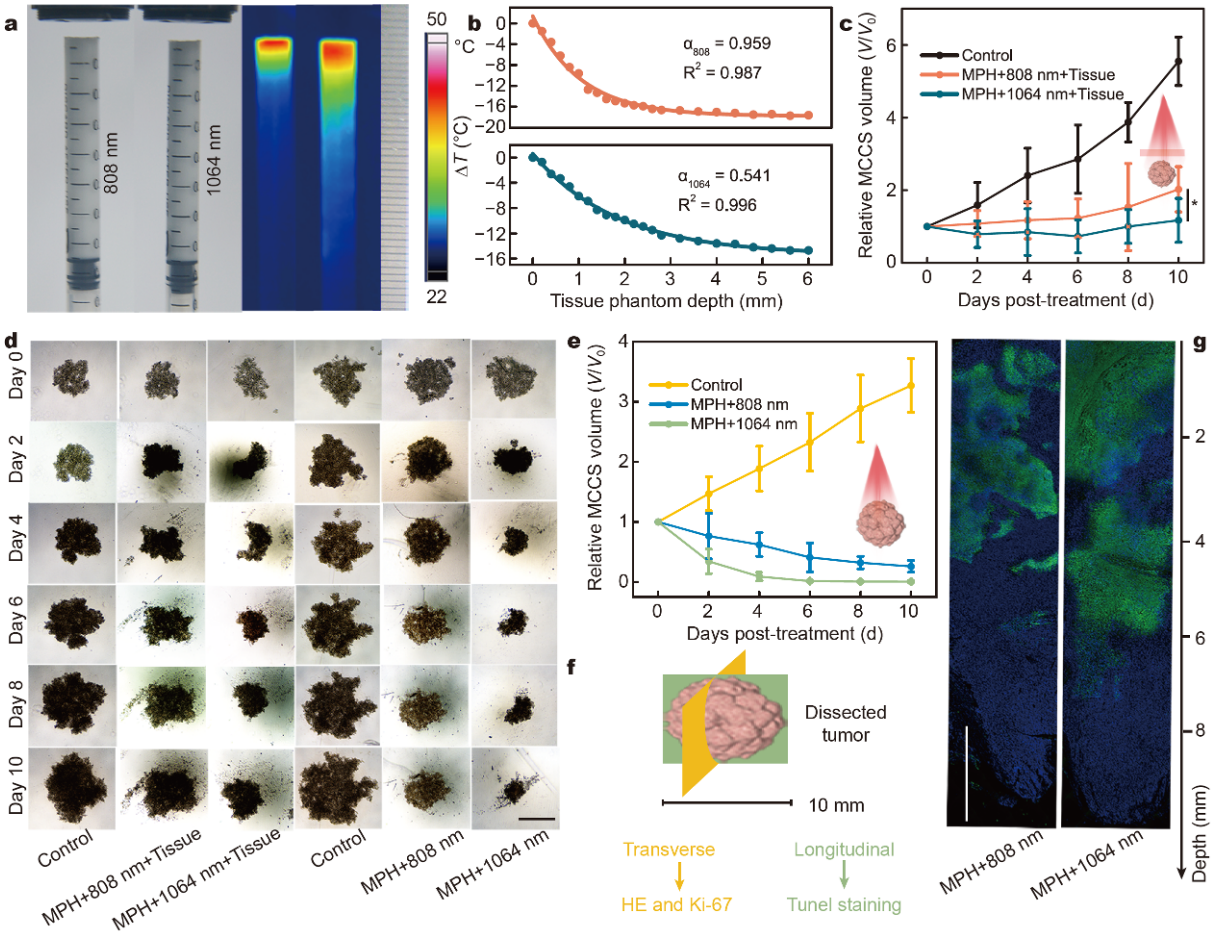

Figure 4 Evaluation of tissue-penetration capability of NIR-I and NIR-II lasers. (a) Photographs and corresponding infrared thermal images of MPH-containing IL tissue phantoms under laser irradiation. (b) Scatter plots of temperature changes through tissue phantoms of different depths, with the fitted attenuation coefficient. (c) Photographs of MCCSs after treatments with or without tissue covering (Scale bar: 500 μm). Mean volume changes of MCCSs after PTT with (d) or without (e) tissue covering. * P<0.05. (f) Schematic diagram of tumor tissue section for staining. (g) TUNEL analysis of longitudinal tumor tissue section at 24 h after treatment (Scale bar: 2 mm). Apoptotic cells are labeled with green fluorescence (FITC) and the living cells are stained with blue fluorescence (DAPI).

decay profiles are then plotted in Fig. 4b, which quantitatively depicts the thermal regression in the tissue phantom. The attenuation coefficients (α) are calculated to be 0.959 and 0.541 for 808 and 1064 nm lasers, respectively, showing obviously higher transmittance of NIR-II laser than NIR-I laser. Next, 3D *in vitro* models were established to further evaluate the photothermal heating ability of NIR laser against deep tumor at cellular levels. Multicellular cancer spheroids (MCCSs) were fabricated and then underwent PTT treatment [41,42]. Fig. 4c–e show the photothermal effect on 3D A549 cell spheroids under NIR-II or NIR-I irradiation with/without a chicken breast tissue (3 mm) coating. It can be clearly noticed that the proliferation of MCCSs is more effectively inhibited by NIR-II irradiation than that by NIR-I exposure whatever the tissue cover, which can be attributed to the intrinsically deeper tissue penetration of NIR-II laser. We also established a 3D gelatin-based scaffold to support cancer cell adhesion and proliferation [32]. The macroscopic photos and SEM microscopic images of the scaffold show a porous 3D network with a mean pore size of about 60 μm that is suitable for cell growth (Fig. S9). Photothermal cancer therapy on 3D cultured A549 cells was then conducted and the fluorescence images of cancer cells stained with Calcein AM (living cells) and PI (dead cells) are exhibited in Fig. S10. A large number of dead cells (red) are discerned in the NIR-II treated 3D tumor model from top to bottom, while the PI-stained cells mostly exist in the superficial zone of scaffold exposed to NIR-I laser. We can also observe the network

 © Science China Press and Springer-Verlag GmbH Germany, part of Springer Nature 2020

structure is severely damaged by 1064 nm laser, suggesting an excellent destruction efficiency of NIR-II PTT on the tumor microenvironment at a multicellular level. Finally, the depth-related photothermal tumor ablation was studied at tissue level. After A549-tumor-bearing mice underwent NIR-I or NIR-II PTT treatment, the tumor tissues were longitudinally and transversely dissected for TUNEL analysis for visual observation on the cell apoptosis along with depth in the tumor (Fig. 4f). Fig. 4g reveals that the effective photothermal damage of subcutaneous xenograft tumor can be obtained at the depth of about 6 mm under a 1064 nm laser, much deeper than the 4 mm observed in 808 nm irradiated tissue. In addition, H&E and Ki-67 immunochemical staining was also executed to study the microstructure alteration and cell proliferation in the tumor tissue at different depths after photothermal treatment (Fig. S11). The results are in accordance with the data above, showing the great promise of using MPH for deep tissue PTT in NIR-II biowindow.

To demonstrate the tissues under PTT more clearly, SERS, a molecular fingerprint analytical technique, was adopted to detect the changes in biochemical components of tumor tissue at different depths. About 400 SERS spectra in each group were obtained from the longitudinal tumor sections. The mean Raman spectral lines of different groups displayed in Fig. 5a possess similar spectral pattern, indicating the fundamental biochemical composition in tumor tissue. However, some SERS bands in the fingerprint spectra change dramatically in response to the laser exposure, such as 728 cm^{-1} (adenine), 760 cm^{-1} (tryptophan), 805 cm^{-1} (O–P–O stretching), 918 cm^{-1} (proline), 1004 cm^{-1} (phenylalanine), 1067 cm^{-1} (C–N stretching in protein, chain C–C stretching in lipid), 1145 cm^{-1} (ribose-phosphate), 1170 cm^{-1} (C–C/C–N stretching in protein), 1376 cm^{-1} (thymine, adenine, guanine), 1586 cm^{-1} (amide II, phenylalanine, tyrosine, adenine, guanine), and 1620 cm^{-1} (C=C olefinic stretching in protein, nucleotide, lipid) [43–46], which may be ascribed to the thermal denaturation induced by the NIR laser. Among them, we can notice that most of these peaks assigned to proteins and nucleotides are attenuated significantly; the vibrational mode of collagen (proline, 918 cm^{-1}) also declines obviously, suggesting both the intracellular and extracellular microstructures of tumor tissues are severely destroyed after laser irradiation. In comparison with MPH+808 nm group, the mean SERS spectrum of tumors that underwent MPH+1064 nm PTT shows more intense fluctuations. The Raman bands at 1145, 1170 and 1376 cm^{-1} decrease 6.1%, 21.0% and 20.1% in the MPH+808 nm group, respectively, while they diminish 27.4%, 35.7% and 62.4% in the MPH+1064 nm group, respectively. The SERS peak at 1620 cm^{-1} that reflects the olefinic bond in the biomolecules endures the most reduction (34.1% and 50.7% decrease in the MPH+808 nm and MPH+1064 nm groups, respectively), which can be ascribed to the thermal instability of C=C band under laser exposure. To elucidate these results clearly, we used a multivariate curve resolution-alternating least square (MCR-ALS) algorithm with 4 components to obtain a loading matrix containing the "pure component" basis spectra (collagen, glycogen,

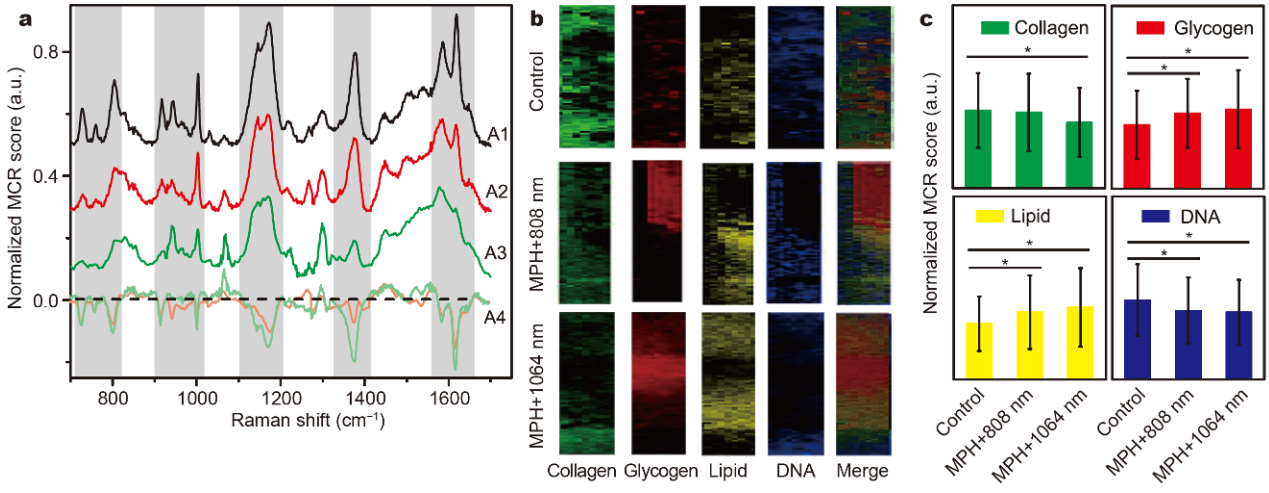

Figure 5 (a) Mean SERS spectra acquired from lung tumors with different treatments. A1: Control; A2: MPH+808 nm; A3: MPH+1064 nm; A4: differences between A1 and A2 or A3 (red: A2−A1; green: A3−A1). (b) MCR-ALS score maps of dissected tumor tissues based on Raman spectroscopic mapping at 24 h after treatment. (c) Mean MCR-ALS scores of the components in tumor after treatment. * $P<0.05$.

© Science China Press and Springer-Verlag GmbH Germany, part of Springer Nature 2020

lipid and DNA, Fig. S12) and a score matrix containing the weights of each of 4 components for all the spectra in the dataset [47,48]. As shown in Fig. 5b, MCR-ALS score maps of the dissected tumor tissue in a control group display a relatively discrete distribution of the four components. However, the degree of dispersion declines and a continuous distribution of some components occurs after PTT, which may reflect the thermal ablation process of tumor tissues. MCR-ALS score of the components in the tumors after different treatments was collected for comparison in Fig. 5c, clearly showing the statistically significant up-regulation of glycogen and lipid as well as down-regulation of collagen and DNA in MPH +808 nm and MPH+1064 nm groups.

To investigate the photothermal property of MPH along with depth, we monitored the photothermal effect on longitudinal tumor tissue sections at interval of 1 mm. The mean SERS spectra of the tumors at different depths before and after treatment are shown in Fig. S13a–c. The difference spectra in Fig. S13d exhibit significant molecular fingerprint changes with depth. The most obvious differences at every depth can be observed in the spectral lines of the MPH+1064 nm group. Next, to quantitatively study the differences across the laser direction, we compared the normalized MCR-ALS scores of lipid-rich, collagen-rich, and glycogen-rich loadings by respective percentages (Fig. S13e). We observe a seriously unbalanced composition of biomolecules at superficial tumor layers after MPH+1064 nm treatment. As the depth increases, the balance gradually returns to the control level. The depth-dependent biochemical composition of tumor tissue after 1064 nm laser irradiation, by the aid of SERS technique, supplies molecule-related knowledge to NIR-II deep-tissue photothermal cancer therapy.

Encouraged by the remarkable deep-tissue photothermal performance, NIR-II PTT on tumor-bearing mice was carried out using MPH as the tumor-targeting photo-responsive nanoagent. Fig. S14 shows the outstanding and stable photothermal capability of MPH under 1064 nm laser at 1 W cm^{-2}. The *in vitro* photothermal cancer-cell ablation capacities of MPH under laser irradiation were then assessed. As shown in Fig. 6a, the relative viability of A549 cells after photothermal ablation illustrates dose-dependent anti-proliferative effects. In comparison with NIR-I therapeutic treatment, NIR-II PTT based on MPH exhibits excellent tumor cell inhibition efficiency at every concentration. Additionally, excellent cell apoptosis after anticancer treatment was further detected by flow cytometer and fluorescence microscope. The cells in control, lasers and MPH groups are negligibly affected, while the tumor cells are partially killed (22.31%) in MPH+808 nm group (Fig. 6b). The maximum apoptotic cell number (37.61%) was noticed after A549 cells were treated with MPH under 1064 nm laser, implying remarkable photothermal therapeutic effects. The efficacy of MPH for *in vivo* NIR-II PTT was studied after targeted systemic administration of MPH *via* tail-vein injection (1 mg kg^{-1}). Under the irradiation by 1064 nm laser (1 W cm^{-2}), the temperature of the tumor region for MPH-treated mice increased rapidly by 25.3°C over 2 min, which was ~3-fold of that in the control group (Fig. 6c, d). To quantitatively assess the antitumor outcome of NIR-II PTT, tumor sizes were recorded continuously for 16 days (Fig. 6e). In contrast to the fast tumor growth in the 1064 nm group, the growth of tumor in MPH+1064 nm group is significantly inhibited, which can be also discerned in the photographs of mice and corresponding tumor dissections, and tumor weights taken at Day 16 after treatment (Fig. 6f–h). H&E staining of tumor tissue displays that no noticeable damage can be observed in tumors from the 1064 nm group, while typical cell nucleus dissociation can be observed in tumors from the MPH+1064 nm group (Fig. 6i), suggesting the apoptosis of cancer cells is triggered by NIR-II PTT. In addition, no evident body weight loss and organ lesions are noticed (Fig. S15), showing the negligible *in vivo* toxic side effects of MPH after NIR-II PTT.

A detailed investigation of the *in vivo* biocompatibility of MPH was further systematically performed. Healthy female BALB/c mice (4–5 weeks old) were intravenously injected with MPH (5 mg kg^{-1}), and then haematological, blood biochemical and histological analyses were carried out at 1, 7 and 16 days post-injection. As shown in Fig. S16a, obvious differences in the standard haematology markers including white blood cells (WBC), red blood cells (RBC), haemoglobin (HGB), mean corpuscular volume (MCV), mean corpuscular haemoglobin (MCH), mean corpuscular haemoglobin concentration (MCHC), platelets (PLT) and haematocrit (HCT) are observed between MPH and control groups at every time point. Similar results are also observed by blood biochemical analysis (blood urea nitrogen (BUN), alanine transaminase (ALT), aspartate transaminase (AST), alkaline phosphatase (ALP), Fig. S16b). These data indicate that MPH does not cause obvious infection and inflammation, or hepatic and kidney toxicity in mice. Finally, the corresponding histological changes in control and MPH groups at 16 days post-injection were checked by H&E staining analysis. No noticeable organ damage can be observed in either group (Fig. S16c), suggesting no

 © Science China Press and Springer-Verlag GmbH Germany, part of Springer Nature 2020

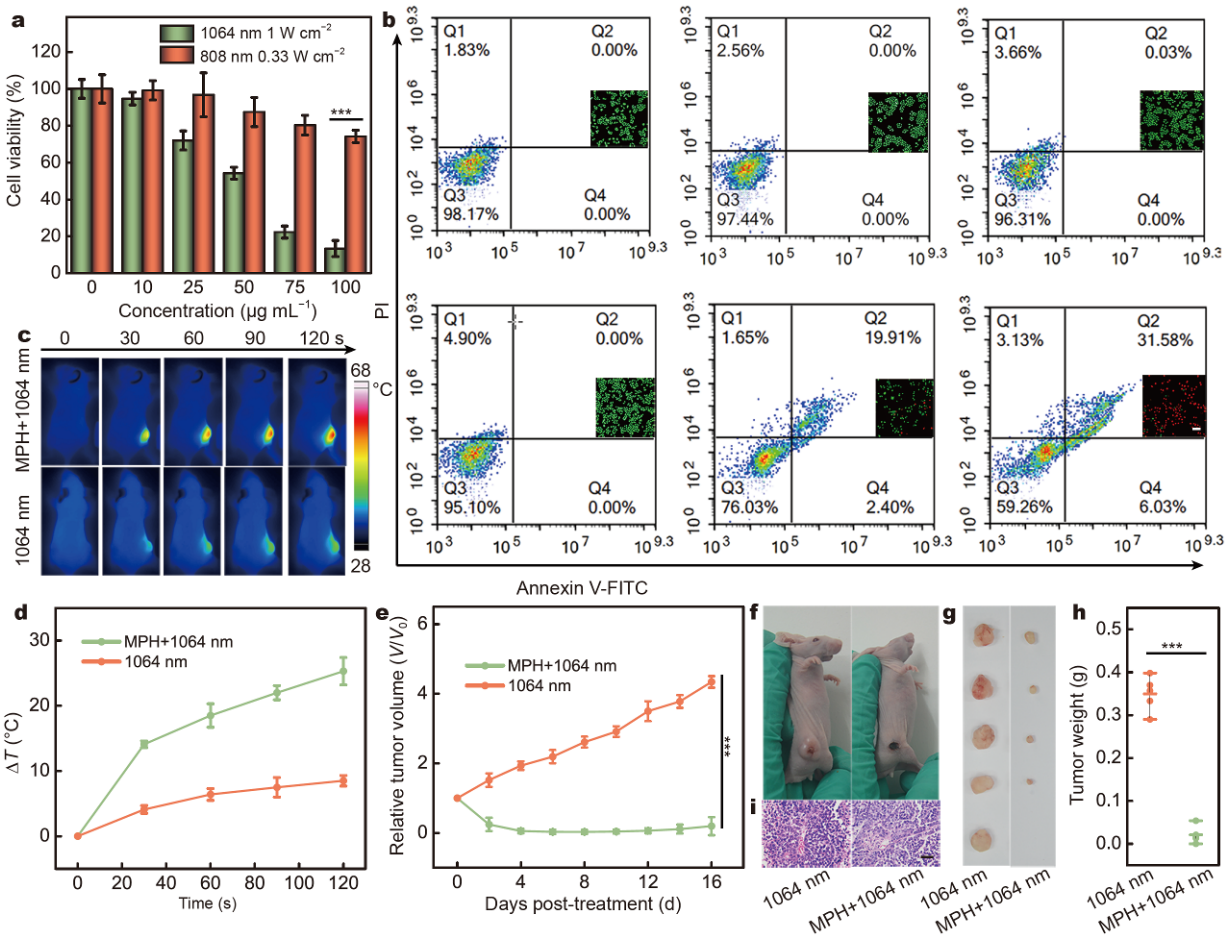

Figure 6 Photothermal cancer therapy in NIR-II window. (a) Relative viability of A549 cells after PTT mediated by MPH at varied concentrations. (b) Cell apoptosis and necrosis analysis of A549 cells with different treatments. Inset: Calcein AM/PI fluorescence imaging of A549 cells after treatment (scale bar: 100 μm). (c) Infrared thermal images of A549-tumor-bearing mice exposed to NIR-II laser after intravenous injection with MPH (1 mg kg^{-1}) or saline. (d) Mean temperature changes of tumors with the treatment time (n = 6). (e) Tumor growth curves in mice after anticancer treatment (n = 5). Photographs of (f) A549-tumor-bearing mice and (g) tumors dissected from mice after treatment, and (h) tumor weights of mice 16 days after treatment (n = 5), along with (i) corresponding H&E staining images in tumor tissue (scale bar: 50 μm). *** P<0.001.

apparent histological abnormalities or lesions in the MPH-treated mice and indicating good *in vivo* biocompatibility of MPH.

CONCLUSIONS

In summary, we have explored a TMO photothermal nanoagent that exhibits wide and strong absorption covering 650–1350 nm as an efficient PTA for NIR-I and NIR-II laser-excited photothermal ablation against tumors. The tumor-targeted MPH exhibits superior PTT efficacy under NIR-II laser irradiation at MPE dose compared with its low wavelength counterpart, suggesting a better alternative for cancer treatment. Finally, the depth profile analysis after PTT reveals the depth-dependent biochemical changes of tumor tissues owing to the ever-attenuating photon energy in deep tissue. We speculate that these efforts to quantify the photothermal-depth correlation during PTT will help broaden more exploration of NIR-II-responsive nanosystems for deep-tumor phototherapy.

Received 24 December 2019; accepted 15 February 2020; published online 19 March 2020

1 Liu FH, Cong Y, Qi GB, *et al.* Near-infrared laser-driven *in situ* self-assembly as a general strategy for deep tumor therapy. Nano Lett, 2018, 18: 6577–6584
2 Yang G, Phua SZF, Lim WQ, *et al.* A hypoxia-responsive albumin-based nanosystem for deep tumor penetration and excellent therapeutic efficacy. Adv Mater, 2019, 31: 1901513
3 Zhang MK, Wang XG, Zhu JY, *et al.* Double-targeting explosible nanofirework for tumor ignition to guide tumor-depth photo-

 © Science China Press and Springer-Verlag GmbH Germany, part of Springer Nature 2020

thermal therapy. Small, 2018, 14: 1800292
4 Bashkatov AN, Genina EA, Kochubey VI, *et al.* Optical properties of human skin, subcutaneous and mucous tissues in the wavelength range from 400 to 2000 nm. J Phys D-Appl Phys, 2005, 38: 2543–2555
5 Plan Sangnier A, Aufaure R, Cheong S, *et al.* Raspberry-like small multicore gold nanostructures for efficient photothermal conversion in the first and second near-infrared windows. Chem Commun, 2019, 55: 4055–4058
6 Liu Y, Zhen W, Wang Y, *et al.* One-dimensional Fe_2P acts as a fenton agent in response to NIR II light and ultrasound for deep tumor synergetic theranostics. Angew Chem Int Ed, 2019, 58: 2407–2412
7 Wang C, Dai C, Hu Z, *et al.* Photonic cancer nanomedicine using the near infrared-II biowindow enabled by biocompatible titanium nitride nanoplatforms. Nanoscale Horiz, 2019, 4: 415–425
8 Ma Q, Cheng L, Gong F, *et al.* Platinum nanoworms for imaging-guided combined cancer therapy in the second near-infrared window. J Mater Chem B, 2018, 6: 5069–5079
9 Yu X, Yang K, Chen X, *et al.* Black hollow silicon oxide nanoparticles as highly efficient photothermal agents in the second near-infrared window for *in vivo* cancer therapy. Biomaterials, 2017, 143: 120–129
10 Li A, Li X, Yu X, *et al.* Synergistic thermoradiotherapy based on PEGylated Cu_3BiS_3 ternary semiconductor nanorods with strong absorption in the second near-infrared window. Biomaterials, 2017, 112: 164–175
11 Alifu N, Zebibula A, Qi J, *et al.* Single-molecular near-infrared-II theranostic systems: ultrastable aggregation-induced emission nanoparticles for long-term tracing and efficient photothermal therapy. ACS Nano, 2018, 12: 11282–11293
12 Feng W, Han X, Wang R, *et al.* Nanocatalysts-augmented and photothermal-enhanced tumor-specific sequential nanocatalytic therapy in both NIR-I and NIR-II biowindows. Adv Mater, 2018, 30: 1805919
13 Zhou J, Jiang Y, Hou S, *et al.* Compact plasmonic blackbody for cancer theranosis in the near-infrared II window. ACS Nano, 2018, 12: 2643–2651
14 Li L, Liu Y, Hao P, *et al.* PEDOT nanocomposites mediated dual-modal photodynamic and photothermal targeted sterilization in both NIR I and II window. Biomaterials, 2015, 41: 132–140
15 Sun T, Dou JH, Liu S, *et al.* Second near-infrared conjugated polymer nanoparticles for photoacoustic imaging and photothermal therapy. ACS Appl Mater Interfaces, 2018, 10: 7919–7926
16 Cao Z, Feng L, Zhang G, *et al.* Semiconducting polymer-based nanoparticles with strong absorbance in NIR-II window for *in vivo* photothermal therapy and photoacoustic imaging. Biomaterials, 2018, 155: 103–111
17 Jiang Y, Li J, Zhen X, *et al.* Dual-peak absorbing semiconducting copolymer nanoparticles for first and second near-infrared window photothermal therapy: a comparative study. Adv Mater, 2018, 30: 1705980
18 Yang Y, Chen J, Yang Y, *et al.* A 1064 nm excitable semiconducting polymer nanoparticle for photoacoustic imaging of gliomas. Nanoscale, 2019, 11: 7754–7760
19 Jiang Y, Upputuri PK, Xie C, *et al.* Metabolizable semiconducting polymer nanoparticles for second near-infrared photoacoustic imaging. Adv Mater, 2019, 31: 1808166
20 Jiang Y, Upputuri PK, Xie C, *et al.* Broadband absorbing semiconducting polymer nanoparticles for photoacoustic imaging in second near-infrared window. Nano Lett, 2017, 17: 4964–4969
21 Chen Y, Tan C, Zhang H, *et al.* Two-dimensional graphene analogues for biomedical applications. Chem Soc Rev, 2015, 44: 2681–2701
22 Chen PC, Shen G, Shi Y, *et al.* Preparation and characterization of flexible asymmetric supercapacitors based on transition-metal-oxide nanowire/single-walled carbon nanotube hybrid thin-film electrodes. ACS Nano, 2010, 4: 4403–4411
23 Gao F, He G, Yin H, *et al.* Titania-coated 2D gold nanoplates as nanoagents for synergistic photothermal/sonodynamic therapy in the second near-infrared window. Nanoscale, 2019, 11: 2374–2384
24 Cheng Y, Yang F, Xiang G, *et al.* Ultrathin tellurium oxide/ammonium tungsten bronze nanoribbon for multimodality imaging and second near-infrared region photothermal therapy. Nano Lett, 2019, 19: 1179–1189
25 Zeng J, Wu M, Lan S, *et al.* Facile preparation of biocompatible Ti_2O_3 nanoparticles for second near-infrared window photothermal therapy. J Mater Chem B, 2018, 6: 7889–7897
26 de Castro IA, Datta RS, Ou JZ, *et al.* Molybdenum oxides—from fundamentals to functionality. Adv Mater, 2017, 29: 1701619
27 Zhan Y, Liu Y, Zu H, *et al.* Phase-controlled synthesis of molybdenum oxide nanoparticles for surface enhanced Raman scattering and photothermal therapy. Nanoscale, 2018, 10: 5997–6004
28 Liu W, Li X, Li W, *et al.* Highly stable molybdenum dioxide nanoparticles with strong plasmon resonance are promising in photothermal cancer therapy. Biomaterials, 2018, 163: 43–54
29 Yin W, Bao T, Zhang X, *et al.* Biodegradable MoO_x nanoparticles with efficient near-infrared photothermal and photodynamic synergetic cancer therapy at the second biological window. Nanoscale, 2018, 10: 1517–1531
30 Song G, Shen J, Jiang F, *et al.* Hydrophilic molybdenum oxide nanomaterials with controlled morphology and strong plasmonic absorption for photothermal ablation of cancer cells. ACS Appl Mater Interfaces, 2014, 6: 3915–3922
31 Song G, Hao J, Liang C, *et al.* Degradable molybdenum oxide nanosheets with rapid clearance and efficient tumor homing capabilities as a therapeutic nanoplatform. Angew Chem Int Ed, 2016, 55: 2122–2126
32 Nguyen TBL, Lee BT. A combination of biphasic calcium phosphate scaffold with hyaluronic acid-gelatin hydrogel as a new tool for bone regeneration. Tissue Eng Part A, 2014, 20: 1993–2004
33 Zhang Q, Li X, Ma Q, *et al.* A metallic molybdenum dioxide with high stability for surface enhanced Raman spectroscopy. Nat Commun, 2017, 8: 14903
34 Huang Q, Hu S, Zhuang J, *et al.* MoO_{3-x}-based hybrids with tunable localized surface plasmon resonances: chemical oxidation driving transformation from ultrathin nanosheets to nanotubes. Chem Eur J, 2012, 18: 15283–15287
35 Ou JZ, Campbell JL, Yao D, *et al.* *In situ* Raman spectroscopy of H_2 gas interaction with layered MoO_3. J Phys Chem C, 2011, 115: 10757–10763
36 Wang YY, Wang WL, Shen XC, *et al.* Combination-responsive MoO_{3-x}-hybridized hyaluronic acid hollow nanospheres for cancer phototheranostics. ACS Appl Mater Interfaces, 2018, 10: 42088–42101
37 Roper DK, Ahn W, Hoepfner M. Microscale heat transfer transduced by surface plasmon resonant gold nanoparticles. J Phys Chem C, 2007, 111: 3636–3641
38 Houghton P, Fang R, Techatanawat I, *et al.* The sulphorhodamine (SRB) assay and other approaches to testing plant extracts and derived compounds for activities related to reputed anticancer activity. Methods, 2007, 42: 377–387
39 Au KM, Lu Z, Matcher SJ, *et al.* Polypyrrole nanoparticles: a po-

 © Science China Press and Springer-Verlag GmbH Germany, part of Springer Nature 2020

tential optical coherence tomography contrast agent for cancer imaging. Adv Mater, 2011, 23: 5792–5795
40 Au KM, Lu Z, Matcher SJ, *et al.* Anti-biofouling conducting polymer nanoparticles as a label-free optical contrast agent for high resolution subsurface biomedical imaging. Biomaterials, 2013, 34: 8925–8940
41 Hirschhaeuser F, Menne H, Dittfeld C, *et al.* Multicellular tumor spheroids: an underestimated tool is catching up again. J Biotech, 2010, 148: 3–15
42 Shield K, Ackland ML, Ahmed N, *et al.* Multicellular spheroids in ovarian cancer metastases: Biology and pathology. Gynecol Oncol, 2009, 113: 143–148
43 Kneipp J, Kneipp H, McLaughlin M, *et al.* *In vivo* molecular probing of cellular compartments with gold nanoparticles and nanoaggregates. Nano Lett, 2006, 6: 2225–2231
44 Thomas GJ, Prescott B, Olins DE. Secondary structure of histones and DNA in chromatin. Science, 1977, 197: 385–388
45 Chan JW, Lieu DK, Huser T, *et al.* Label-free separation of human embryonic stem cells and their cardiac derivatives using Raman spectroscopy. Anal Chem, 2009, 81: 1324–1331
46 Liu Z, Chen H, Jia Y, *et al.* A two-dimensional fingerprint nanoprobe based on black phosphorus for bio-SERS analysis and chemo-photothermal therapy. Nanoscale, 2018, 10: 18795–18804
47 Paidi SK, Rizwan A, Zheng C, *et al.* Label-free Raman spectroscopy detects stromal adaptations in premetastatic lungs primed by breast cancer. Cancer Res, 2017, 77: 247–256
48 Paidi SK, Diaz PM, Dadgar S, *et al.* Label-free Raman spectroscopy reveals signatures of radiation resistance in the tumor microenvironment. Cancer Res, 2019, 79: 2054–2064

Acknowledgements This work was supported by the National Natural Science Foundation of China (11874021, 61675072, 81601534 and 51402207), the Science and Technology Project of Guangdong Province of China (2017A020215059), and the Science and Technology Project of Guangzhou City (201904010323).

Author contributions Zu H designed and characterized the samples with support from Hu C; Guo Y modified the samples and performed the experiments with the help of Li Y, Yu H and Li D; Zhang W processed the Raman data to be decoded; Xiong H contributed to the theoretical analysis; Guo Y wrote the paper with support from Liu Z, Hu C, Hormel TT and Guo Z. All authors contributed to the general discussion.

Conflict of interest The authors declare that they have no conflict of interest.

Supplementary information Supporting data are available in the online version of the paper.

Yanxian Guo received her BSc degree from Harbin Medical University (China) in 2016 and MSc from the South China Normal University. She is currently a PhD student in Prof. Zhouyi Guo's group at the South China Normal University. Her main research focuses on the synthesis of 2D nanomaterials and their applications for cancer theranostics.

Chaofan Hu received his BSc degree from Hebei Polytechnic University in 2007, MSc degree from the South China Normal University in 2010, and PhD degree from Jinan University in 2013, and then joined Taiyuan University of Technology as a lecturer. Currently, he is an associate professor at the South China Agricultural University. His research interests include the syntheses of luminescent nanomaterials and their bio-applications.

Zhouyi Guo is currently a full professor in the College of Biophotonics at South China Normal University. His current research focuses on nanomaterials, biosensors, and bioimaging.

Zhiming Liu is an associate professor in MOE Key Laboratory of Laser Life Science & Institute of Laser Life Science in South China Normal University. His current research is focused on cancer research based on nanotechnology, nanobiology and Raman spectrometry analysis.

基于肿瘤靶向MoO_2纳米聚集体的近红外区深组织光热治疗

郭艳先[1], 李阳[1], 张沃伦[1], 祖鸿儒[2], 余海红[1], 李东铃[1], 熊红莲[3], Tristan T. Hormel[4], 胡超凡[2*], 郭周义[1*], 刘智明[1*]

摘要 近红外II区(NIR-II, 1000–1350 nm)的光热治疗(PTT)近年来发展迅速，其最大允许照射量和组织穿透深度均高于近红外I区(NIR-I, 650–950 nm). 金纳米结构、单壁碳纳米管、钯纳米颗粒等材料已作为高效的NIR-II光热消融肿瘤的治疗剂被探索，而关于NIR-II PTT后的深部组织转化的细节信息还有待发掘. 本文系统地研究了NIR-II深层组织PTT术后肿瘤的深度分布. 基于NIR响应的氧化钼(MoO_2)纳米聚集体的肿瘤靶向治疗纳米系统，我们开展了光热肿瘤治疗. 为了验证PTT后的组织深度相关细节，我们建立了三个不同层次的模型：组织模型、三维细胞系统模型与荷瘤动物模型. NIR-II激光在组织模型中表现出较低的光热衰减系数(1064 nm时为0.541)，而在808 nm时该值为0.959，这使得它在体内外都能更好地进行深层组织PTT. 深度剖面分析表明肿瘤组织的显微结构破坏与穿透深度呈负相关. 同时，我们利用拉曼光谱对PTT后组织深度图谱的生化指纹变化进行解码，揭示了光热消融肿瘤组织中主要的生化成分紊乱，为NIR-II深层组织光热治疗提供了理论基础.

 © Science China Press and Springer-Verlag GmbH Germany, part of Springer Nature 2020